

First-principles calculation of highly asymmetric structure in scanning-tunneling-microscopy images of graphite

David Tománek* and Steven G. Louie

*Department of Physics, University of California, Berkeley, California 94720
and Center for Advanced Materials, Lawrence Berkeley Laboratory, Berkeley, California 94720*

(Received 13 July 1987)

Using a first-principles calculation, we have computed the charge density for states near E_F that is related to the current density observable in scanning-tunneling-microscopy experiments for surfaces of hexagonal, rhombohedral, and a model stage-1 intercalated graphite. In hexagonal and rhombohedral graphite, the tunneling current is predicted to be considerably smaller at surface atomic sites which have nearest neighbors directly below them than at sites with no such neighbors. This asymmetry is explained by the particular symmetry of the wave functions at the Fermi surface of graphite near \bar{K} in the surface Brillouin zone. The calculated asymmetry is nearly independent of the polarity and decreases with increasing magnitude of the bias voltage. Our results show that no asymmetry is expected on surfaces of stage-1 AA stacked intercalated graphite. The dependence of the asymmetry on the tip-to-surface separation has also been evaluated using a tight-binding model for different bias voltages. For the surface of hexagonal graphite, our predictions have been confirmed by recent experiments.

I. INTRODUCTION

Since its invention,¹ scanning tunneling microscopy (STM) has proven to be a powerful technique in viewing the surface structure of various systems with atomic resolution. In this technique, a small bias voltage V is applied between a sample and an "atomically sharp" metal tip, which yields a tunneling current I at typical tip-to-surface separations of several angstroms. Depending on the polarity of V , the tunneling occurs by transfer of electrons either from occupied states of the sample into unoccupied states of the tip, or from the tip to the sample. In the topographic mode of STM operation,¹ a feedback mechanism changes the tip-to-surface separation in order to keep the tunneling current constant. The STM image is then given by recording the distance changes during a scan of the surface. In the alternative current-imaging mode,² an STM image is constituted by recording the tunneling current, as the tip rapidly scans the surface at a constant distance.

At bias voltages which range typically between 0 and 1 V, the tunneling current is sensitive to the character of the electronic states of the sample near the Fermi energy. In many systems, the charge distribution of these states is characteristic of the total charge density and the STM images give a view of the atomic arrangement at the surface. On the other hand, it should not be surprising that in systems with a Fermi surface containing a limited number of states of specific character—such as graphite—the observed images can look very different from what the atomic structure would suggest. A considerable amount of effort has been devoted to studies of graphite,^{2–5} partly due to the ease of preparing surfaces which are atomically flat over hundreds of angstroms. These studies revealed two anomalous features: "giant corrugations" (enormous apparent heights of atoms

above the centers of the carbon rings)^{2–5} and a substantial asymmetry in the apparent heights of neighboring carbon sites.^{4,5} Neither of these features can be understood within the simplistic picture that the STM images atomic structure at the surface.

The "giant" corrugations of up to 24 Å between the atomic sites and the center of the carbon hexagons have been observed on graphite surfaces in air in the topographic mode.⁵ This feature in the STM image has been attributed to elastic interactions between the tip and the graphite surface⁶ or, alternatively, to the presence of a node at the center of the hexagons for wave functions of the electronic states at the Fermi surface of a graphite layer.⁷ A combination of these effects has been shown to be responsible for the extremely large corrugations observed when the STM was operated in the topographic mode in air.⁵ Under these conditions, the corrugations induced by the electronic structure were strongly amplified by elastic interactions between the tip and the surface through a layer of contamination. It has further been shown⁵ that this amplification of corrugations disappears if the STM is operated either in vacuum or in the current-imaging mode, where elastic deformation remains nearly constant during one scan.

The second anomaly, a large asymmetry in the tunneling current between adjacent sites on the (0001) surface of hexagonal graphite, has been recently explained by the unique symmetry of the states near the \bar{K} point in the surface Brillouin zone near the Fermi energy.⁸ This effect has an electronic rather than a topographic origin. The quantitative calculation predicted a bias-voltage dependence of the asymmetry which was confirmed by experiment. In this paper we give the details of that calculation, extend it to the surfaces of rhombohedral and a model stage-1 intercalated graphite (with AA layer stacking), and make comparison to bulk results.

The paper is structured as follows. In Sec. II we present the *ab initio* calculation of the expected STM current densities. In Sec. III we outline the underlying physics by using a simple tight-binding model. Finally, in Sec. IV we discuss our results and present conclusions.

II. CALCULATION OF STM IMAGES OF GRAPHITE

Applying a small bias voltage V between the sample and the tip yields a tunneling current, whose density $j(\mathbf{r})$ can be obtained from a simple extension⁹ of the expression derived by Tersoff and Hamann,¹⁰

$$j(\mathbf{r}, V) \propto \rho_{\text{STM}}(\mathbf{r}, V), \quad (2.1)$$

where

$$\rho_{\text{STM}}(\mathbf{r}, V) \equiv \int_{E_F - eV}^{E_F} dE \rho(\mathbf{r}, E) \quad (2.2a)$$

and

$$\rho(\mathbf{r}, E) \equiv \sum_{n, \mathbf{k}} |\psi_{n\mathbf{k}}(\mathbf{r})|^2 \delta(E_{n\mathbf{k}} - E). \quad (2.2b)$$

Here, $\rho(\mathbf{r}, E)$ is the local density of states at the center of curvature of the tip $\mathbf{r} = (x, y, z)$ and $\psi_{n\mathbf{k}}(\mathbf{r})$ are the electron eigenstates of the unperturbed surface with corresponding energy $E_{n\mathbf{k}}$. The implied assumptions^{9,10} are the following. The description of the relevant tip states is by s waves with a constant density of states. The tunneling matrix element is independent of the lateral tip position for a constant tip-to-surface distance, and also is independent of the bias voltage V in the narrow (but nonzero) energy region $[E_F - eV, E_F]$.

Using this model, the current density $j(\mathbf{r}, V)$ depends sensitively on the nature of the wave functions $\psi_{n\mathbf{k}}$ of the states near the Fermi energy. The electron energies and wave functions are obtained by solving self-consistently the Kohn-Sham equations within the density-functional formalism,^{11,12}

$$\left[-\frac{\hbar^2}{2m} \nabla^2 + V_{\text{ext}} + V_H[\rho] + V_{\text{xc}}[\rho] \right] \psi_{n\mathbf{k}} = \epsilon_{n\mathbf{k}} \psi_{n\mathbf{k}} \quad (2.3a)$$

and

$$\rho(\mathbf{r}) = \sum_{n, \mathbf{k}}^{\text{occ}} |\psi_{n\mathbf{k}}(\mathbf{r})|^2. \quad (2.3b)$$

Here, V_{ext} is an external potential due to the ions, V_H is the Hartree potential, and V_{xc} is the exchange-correlation potential for the charge density $\rho(\mathbf{r})$. In our calculation, only the valence charge density is considered, and V_{ext} is replaced by a first-principles ionic pseudopotential, which combines the nucleus and the core electrons into one entity.

To solve the Kohn-Sham equations, we use the *ab initio* pseudopotential local-orbital method (PLOM) (Ref. 13) which determines self-consistently the plane-wave components of the charge density and the potential up to an energy of 49 Ry. The basis consists of local Gaussian-type orbitals of the form

$$f_{alm}(\mathbf{r}) = A_{alm} e^{-\alpha r^2} K_{lm}(\theta, \phi), \quad (2.4)$$

which are localized on atomic sites. A_{alm} are normalization constants and K_{lm} are the Kubic harmonics $\{1, x, y, z\}$ for $l=0, 1$. For each site, we consider s , p_x , p_y , and p_z orbitals with three radial Gaussian decays α each, i.e., 12 independent basis functions. This basis is complemented by four long-range Gaussians located at half the interlayer distance above and below each carbon atom. We find that extending our local basis set using floating orbital sites in the interlayer region proves useful in describing the unoccupied interlayer states¹⁴ correctly, but does not modify our STM results. The decays, which minimize the total energy, are^{15,16} $\alpha = 0.24, 0.797$, and 2.65 . We use norm-conserving ionic pseudopotentials of the Hamann-Schlüter-Chiang type¹⁷ and the Hedin-Lundqvist¹⁸ form of the exchange-correlation potential in the local density approximation.

The total energy of the system is obtained as a by-product of our density-functional calculations. We find that the total energy per atom of a four-layer rhombohedral graphite slab agrees up to 0.01 eV with the result of a previous calculation of bulk graphite¹⁵ with the same intralayer and interlayer spacing, which confirms the completeness of our basis. Total energy differences of less than 0.005 eV per atom are obtained in graphite slabs with different stacking (*AA*, *ABAB*, and *ABC*) but with the same interlayer and intralayer distances. This is a further indication of the weak interlayer interaction.

Our calculation is performed in two steps. First, the self-consistent potential is determined using a uniform grid of \mathbf{k} points, which sample the irreducible part of the Brillouin zone (BZ). In a second step, given a self-consistent potential, the STM charge density $\rho_{\text{STM}}(\mathbf{r}, V)$ is obtained from Eq. (2.2) by summing up the contributions point by point for a much finer \mathbf{k} -point mesh.

A. Hexagonal graphite

Hexagonal graphite (with *ABAB* stacking of layers) is the most common form of graphite in nature. The atomic arrangement and the bulk unit cell are shown in Figs. 1(a) and 1(b). The in-layer nearest-neighbor carbon distance is 1.42 Å and carbon layers are separated by 3.35 Å.

In the calculation of bulk hexagonal graphite, the self-consistent potential and charge density are generated by sampling the irreducible part of the three-dimensional BZ [Fig. 2(a)] using a uniform mesh of 57 \mathbf{k} points. For the surface, which is represented by a four-layer slab, the analogous calculation is performed for a seven \mathbf{k} -point set in the surface BZ [Fig. 2(b)]. The Fermi surface lies close to the P line in the bulk BZ and to the \bar{K} point in the surface BZ.

The calculation of STM charge densities $\rho_{\text{STM}}(\mathbf{r}, V)$ is performed by sampling the \mathbf{k} -space region near the Fermi surface by a very fine mesh of 610 \mathbf{k} points and 61 \mathbf{k} points in the irreducible parts of the bulk and surface BZ, respectively. Not all \mathbf{k} points contribute to $\rho_{\text{STM}}(\mathbf{r}, V)$, since the portion of the band structure sampled by the STM is very small for typical tunneling voltages below

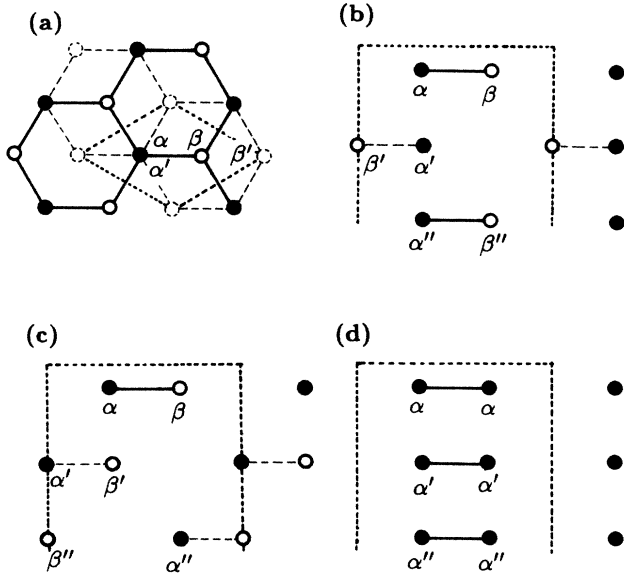


FIG. 1. Schematic drawing of the atomic arrangement in hexagonal graphite, top view (a) and side view (b). Side view of the atomic arrangement in rhombohedral graphite (c) and model stage-1 intercalated graphite (d). The surface unit cells are enclosed by a dashed line.

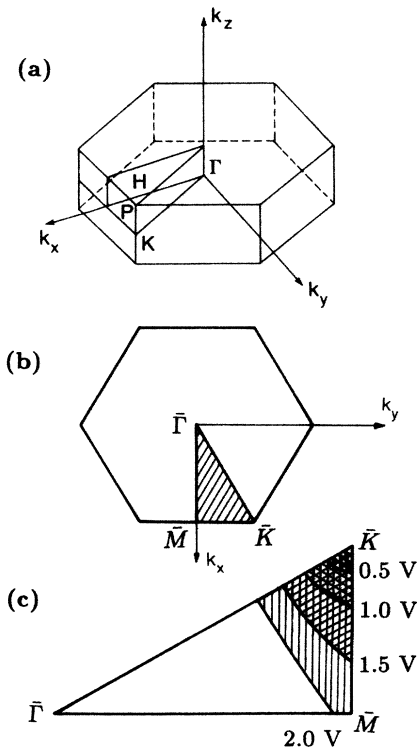


FIG. 2. (a) Bulk and (b) surface Brillouin zones (BZ's) of hexagonal graphite. (c) Fraction of the surface BZ, which is sampled at different bias voltages.

1 V. For the surface, the V dependence of this portion of the BZ is shown in Fig. 2(c). In order to reduce the influence of the slab thickness on the surface results, we derive a k_{\parallel} -resolved density of states from the four-layer slab results by broadening energy levels using Gaussians with a half-width at half maximum of 0.2 eV. This width is smaller than the energy level spacing of ≈ 0.4 V at \bar{K} .

In Fig. 3(a), we present our results for the total charge density of hexagonal graphite in a plane perpendicular to the layers. As seen from the figure, no discernible charge-density asymmetry is observed and the charge distribution reproduces the atomic structure, which is shown schematically in Fig. 1(b).

The charge density observed by the STM in a narrow energy region at E_F , as defined by Eq. (2.2a), looks considerably different. The behavior of this quantity on a hexagonal graphite surface is shown in Fig. 4 for a tunneling voltage of 0.25 V, together with experimental data from Ref. 8. The side view in a plane perpendicular to the graphite layers, given in Fig. 4(a), shows that at low bias voltages the STM images mostly the p_z states on the carbon atoms. The current density has a considerable asymmetry between the α sites [atoms with neighbors in the adjacent layer below, see Fig. 1(b)] and the β sites (atoms with no such neighbors). Figure 4(b) represents the tunneling current density on a gray scale, as observed by an ideal tip 1 Å above the surface. The areas of high tunneling current, shown as white spots in the image, form a hexagonal close-packed array, as observed in the experiment [Fig. 4(d)]. The agreement between theory and experiment can be considerably improved, if the finite resolution of the real tip is taken into account.¹⁹ In our case, this has been done by filtering out the high-frequency Fourier components of the "ideal" current density with a Gaussian. The filtered STM charge density, presented in Fig. 4(c), indeed shows a remarkable agreement with the experimental data.

The dependence of the tunneling current density on the bias voltage is demonstrated in Fig. 5 for hexagonal graphite. The STM charge density given by Eq. (2.2) is evaluated 1 Å above the graphite layer in the bulk and at the same separation from the topmost layer at the surface. Both the surface and the bulk results show the same trend, a strong decrease of the asymmetry with increasing bias voltage. Moreover, for small bias voltages below ≈ 0.5 V, the calculated asymmetries are almost independent of the polarity of the bias.

This behavior can be quantified by defining the asymmetry A between the STM charge density ρ_{STM} at the α and β sites by

$$A \equiv \frac{\rho_{\text{STM}}(\beta) - \rho_{\text{STM}}(\alpha)}{\rho_{\text{STM}}(\beta) + \rho_{\text{STM}}(\alpha)}. \quad (2.5)$$

The bias-voltage dependence of A for the surface of hexagonal graphite is shown in Fig. 6, for two different tip-to-surface separations. From our results, we observe no strong dependence of the asymmetry on the tip-to-surface separation in the limited range 0.5–1 Å although in this range there is a strong decrease of the charge density. The dependence of A on distance will be discussed in

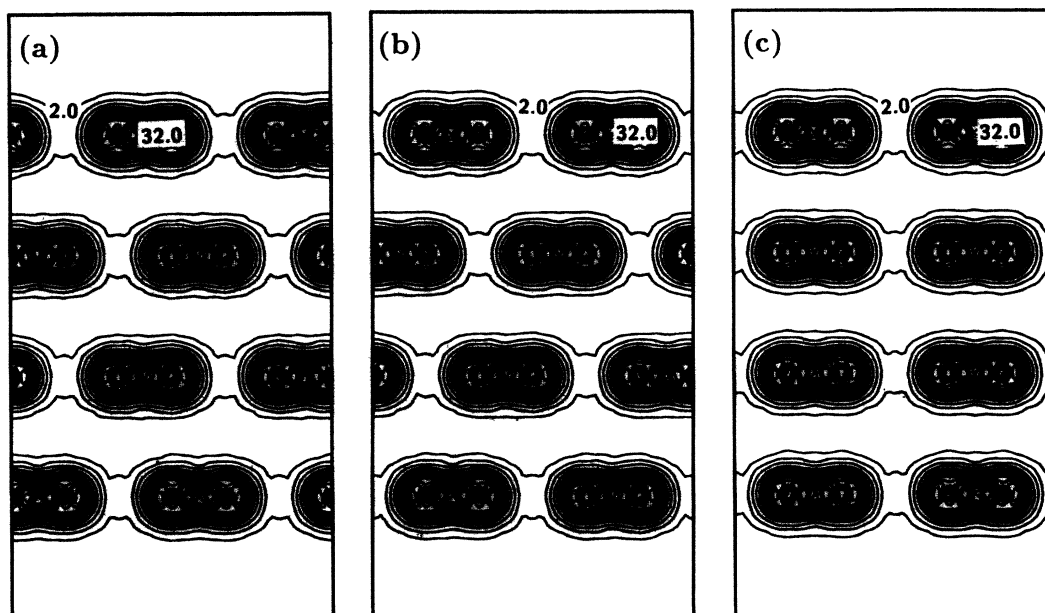


FIG. 3. Total charge densities for a four-layer slab of hexagonal graphite (a), rhombohedral graphite (b), and model stage-1 intercalated graphite (c), viewed in a plane perpendicular to the graphite layers. Charge density is given in units of 10^{-2} electrons/a.u.³; consecutive contours are separated by 2×10^{-2} electrons/a.u.³.

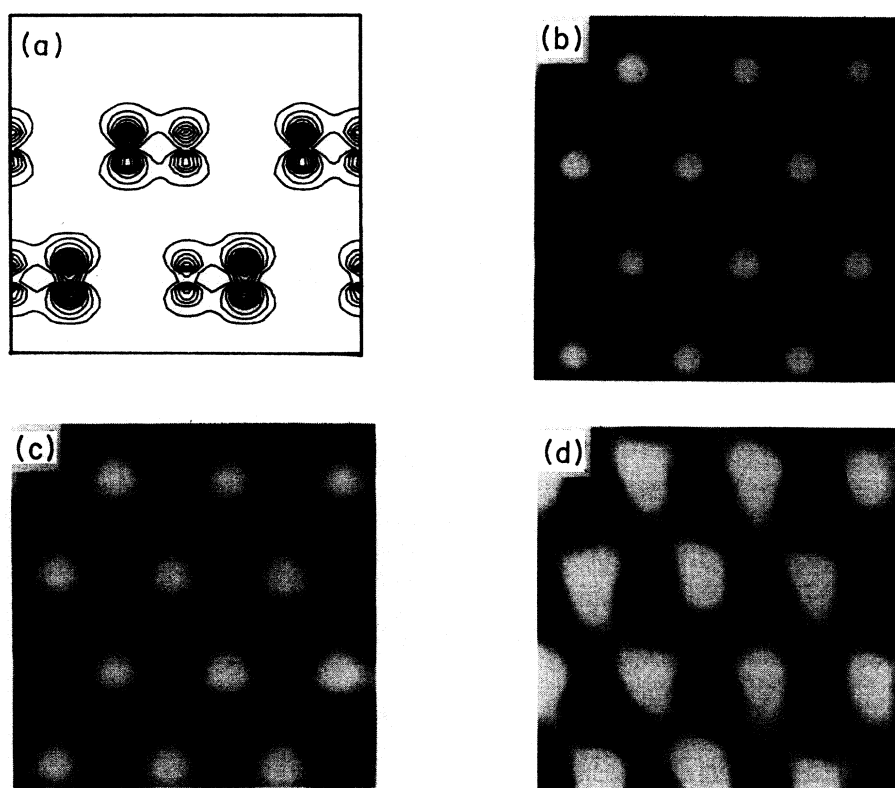


FIG. 4. Comparison of theoretical STM charge density to experimental tunneling current density at hexagonal graphite surfaces for a bias voltage of 0.25 V. Calculated values are shown in a plane perpendicular (a) and parallel (b) to the graphitic layers at a distance 1 Å from the topmost layer. (c) is obtained by filtering high-frequency Fourier components of the charge density of (b) with a Gaussian, can be compared to experimental data from Ref. 8, shown in (d). On the gray scale, white regions correspond to large current densities.

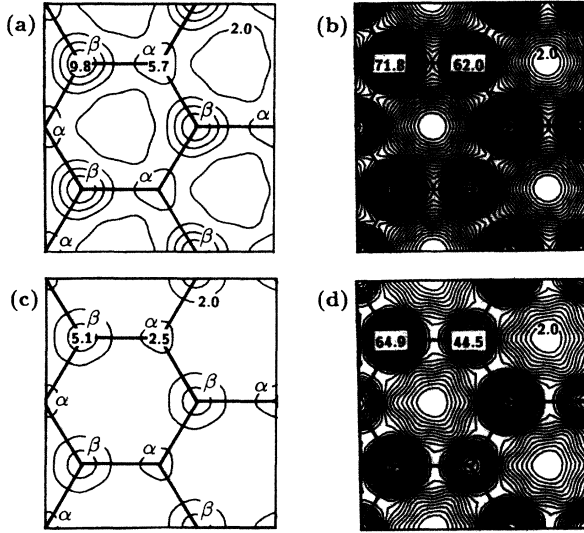


FIG. 5. Contour plots of the STM charge density ρ_{STM} for hexagonal graphite, in a plane parallel to and 1 Å above a bulk layer and above the topmost surface layer. Surface results for ρ_{STM} are given for bias voltages $V = 0.2$ V (a) and 0.8 V (b). The units are 10^{-3} electrons/a.u.³, consecutive contours are separated by 2×10^{-3} electrons/a.u.³. Bulk results (c) and (d) are obtained for the same bias voltage as (a) and (b), respectively. They are given in units of 10^{-4} electrons/a.u.³ with consecutive contours separated by 2×10^{-4} electrons/a.u.³.

more detail in Sec. IV. Filtered theoretical values for A , which include the effect of a finite experimental resolution, are given by the dotted curve in Fig. 6. The same filter parameters have been used for all voltages and correspond to those used in Fig. 4(c). We further note that h was almost certainly greater than 1 Å in the experiment;

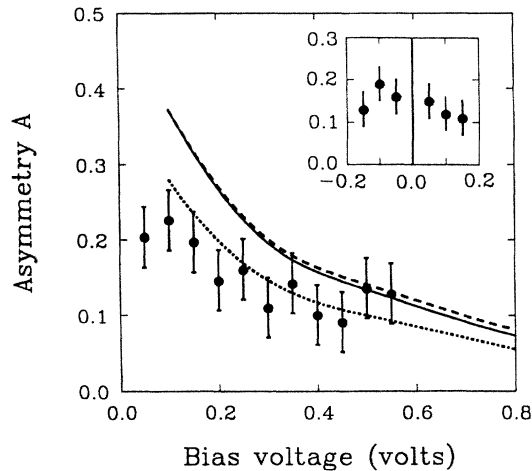


FIG. 6. Asymmetry $A \equiv [j(\beta) - j(\alpha)] / [j(\beta) + j(\alpha)]$ of the tunneling current j as a function of the bias voltage V for a hexagonal graphite surface. The solid and dashed lines represent calculated results at a tip-surface separation $h = 1$ Å and 0.5 Å, respectively. The dotted line represents theoretical data at 1 Å, which have been filtered to mimic the finite experimental resolution. The experimental points are constant resistance data from Ref. 8, corresponding to an unknown value of h . The inset shows the observed polarity dependence of A .

if so, A would be further reduced below the computed values. The experimental data points from Ref. 8, shown in the same figure, were obtained by averaging over the current densities on the “more” visible and the “less” visible atoms on the surface²⁰ over the scanned area. They show a less pronounced trend of decreasing asymmetry with increasing bias voltage as compared to the theoretical data.

B. Rhombohedral graphite

Rhombohedral graphite (with ABC stacking sequence of layers) is often found intermixed with the hexagonal and the disordered phase in natural graphite.²¹ A side view of the structure is given in Fig. 1(c). The in-plane nearest-neighbor distances and the interlayer separation are indistinguishable from those in hexagonal graphite. The Fermi surface is again very close to the \bar{K} point in the surface BZ, which is identical to that of hexagonal graphite shown in Fig. 2(b).

Unlike in hexagonal graphite, all atoms are equivalent in the bulk and there is no charge-density asymmetry. At the surface, however, we can distinguish α sites with neighbors directly below and β sites with no such neighbors [Fig. 1(c)]. Although this site inequivalence causes almost no asymmetry in the total charge density [Fig. 3(b)], there is a considerable asymmetry in the STM charge density ρ_{STM} , especially at low bias voltages. As we discuss in more detail in Sec. III, unlike hexagonal graphite, this asymmetry is caused by a surface state at \bar{K} , which lies at E_F and which is localized on β atoms. We calculated the bias-voltage dependence of A using a fine k -point mesh of 61 k points and checked our results using an 817 k -point set in the irreducible part of the surface Brillouin zone, which corresponds to 9073 k points in the full BZ. This fine k -point mesh is essential for quantitative results in rhombohedral graphite, since the system has a direct gap which closes nearly to zero away from \bar{K} . Our results for the asymmetry as a function of bias voltage are shown in Fig. 7.

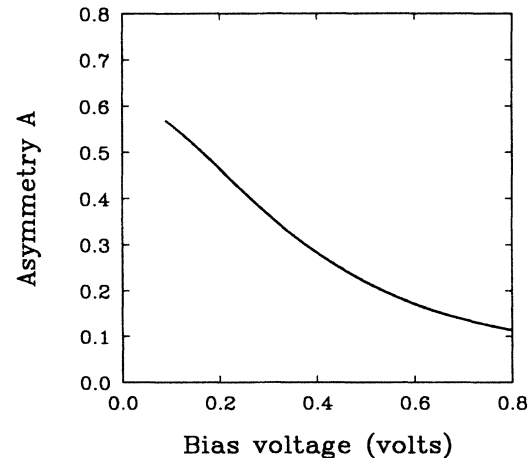


FIG. 7. Predicted asymmetry A of the tunneling current j as a function of the bias voltage V for a rhombohedral graphite surface, obtained for a tip-surface separation $h = 1$ Å.

C. Stage-1 intercalated graphite

Many stage-1 intercalated graphite compounds show an *AA* stacking of layers. In the case of Li intercalate, the in-plane atomic bond lengths are expanded by 1% and the intralayer separation is expanded by 10% as compared to hexagonal graphite.²² A side view of the structure is given in Fig. 1(d). To a good approximation, the electronic effect of Li intercalation near E_F is an upward shift of the Fermi energy by 1 eV.

Since all atoms are equivalent in the bulk and at the surface, no asymmetry is expected in the total nor in the STM charge densities. This is confirmed by our calculation, which uses a rigid band model with an expanded crystal in the *AA* stacking. The \mathbf{k} -point sampling of the BZ is the same as that of hexagonal graphite. Our result for the total charge density is given in Fig. 3(c). Also, as expected, the STM charge densities (not given in a figure) do not show any asymmetry between adjacent sites.

III. INTERPRETATION OF TUNNELING CURRENT DENSITIES ON GRAPHITE

To understand the calculated *ab initio* results presented in Sec. II, we discuss here the underlying physics by use of a simple tight-binding Hamiltonian. We show that all our results can be qualitatively understood from the nature of the wave functions $\psi_{n\mathbf{k}}$ near the Fermi surface of graphite, which determine the current density by means of the relations given in Eqs. (2.1) and (2.2).

A. Hexagonal graphite

For the sake of simplicity, we start with the discussion of bulk hexagonal graphite. Band-structure calculations of hexagonal graphite¹⁴ show that the eigenstates $\psi_{n\mathbf{k}}$ needed in Eq. (2.2), which contribute to the tunneling current, are mainly p_z in character and can be well approximated as a linear combination of Bloch functions Φ_j localized on the α , α' , β , and β' atomic sites in the unit cell shown in Fig. 1(b),

$$\psi_{n\mathbf{k}}(\mathbf{r}) = c_{n\alpha}(\mathbf{k})\Phi_{\alpha}(\mathbf{r}, \mathbf{k}) + c_{n\alpha'}(\mathbf{k})\Phi_{\alpha'}(\mathbf{r}, \mathbf{k}) + c_{n\beta}(\mathbf{k})\Phi_{\beta}(\mathbf{r}, \mathbf{k}) + c_{n\beta'}(\mathbf{k})\Phi_{\beta'}(\mathbf{r}, \mathbf{k}), \quad (3.1)$$

where

$$\Phi_j(\mathbf{r}, \mathbf{k}) = \frac{1}{\sqrt{N}} \sum_{\mathbf{R}} e^{i\mathbf{k} \cdot (\mathbf{R} - \tau_j)} p_z(\mathbf{r} - \mathbf{R} + \tau_j), \quad j = \alpha, \alpha', \beta, \beta'. \quad (3.2)$$

The Fermi surface of graphite lies close to the *P* line in the bulk Brillouin zone [Fig. 2(a)], defined by $\mathbf{k} = (\frac{1}{3}, \frac{1}{3}, \xi)$ (in units of reciprocal-lattice vectors). To obtain the energy and the wave functions of the electrons along this line, the matrix elements of the Hamilton operator $H_{ij}(\mathbf{k}) = \langle \Phi_i | H | \Phi_j \rangle$ can be evaluated in the nearest-neighbor approximation as follows.

The on-site energies of p_z states on α and β atoms are given by

$$H_{\alpha\alpha} = E_{\alpha} \quad (3.3a)$$

and

$$H_{\beta\beta} = E_{\beta}. \quad (3.3b)$$

Since the crystal field on α and β sites is very similar, we set $E_{\alpha} = E_{\beta} = E_{p_z}$. The off-diagonal matrix elements H_{ij} are calculated by evaluating

$$H_{ij} = \sum_{\mathbf{R}} e^{i\mathbf{k} \cdot (\mathbf{R} + \tau_i - \tau_j)} \int d^3r p_z(\mathbf{r} - (\mathbf{R} - \tau_i + \tau_j)) H p_z(\mathbf{r}). \quad (3.4)$$

When evaluating the in-plane interactions between the α and β sublattices, we note that in the nearest-neighbor approximation, the sum in Eq. (3.4) contains only three nonvanishing terms due to the three β neighbors of an α site. Defining $\delta_{\alpha\beta} \equiv \mathbf{R} + \tau_i - \tau_j$, the corresponding vectors $\delta_{\alpha\beta}$ are $\delta_{\alpha\beta,1} = (\frac{2}{3}, \frac{1}{3}, 0)$, $\delta_{\alpha\beta,2} = (-\frac{1}{3}, -\frac{2}{3}, 0)$, and $\delta_{\alpha\beta,3} = (-\frac{1}{3}, \frac{1}{3}, 0)$ (in units of Bravais lattice vectors). For $\mathbf{k} = (\frac{1}{3}, \frac{1}{3}, \xi)$, the phase factors in Eq. (3.4) are $e^{i\mathbf{k} \cdot \delta_{\alpha\beta,1}} = e^{+i2\pi/3}$, $e^{i\mathbf{k} \cdot \delta_{\alpha\beta,2}} = e^{-i2\pi/3}$, and $e^{i\mathbf{k} \cdot \delta_{\alpha\beta,3}} = 1$, and the hopping integrals $V_{\alpha\beta}$ are the same. Then,

$$H_{\alpha\beta} = (e^{+i2\pi/3} + e^{-i2\pi/3} + 1)V_{\alpha\beta} = 0 \quad (3.5a)$$

and similarly

$$H_{\alpha'\beta'} = 0. \quad (3.5b)$$

Hence, states on α and β sites in the same plane do not mix at the *P* line. Since the same argument also holds for the second, third, etc. β nearest neighbors of an α site, the results in Eqs. (3.5a) and (3.5b) are in fact exact to all orders of neighbor interactions.

The same line of arguments yields that, at the *P* line, p_z orbitals on β sites are decoupled from those on both α and β sites in adjacent layers, resulting in

$$H_{\alpha\beta'} = 0, \quad (3.5c)$$

$$H_{\alpha'\beta} = 0, \quad (3.5d)$$

and

$$H_{\beta\beta'} = 0. \quad (3.5e)$$

This result is also valid to all orders of neighbor interactions. Since the argument does not depend on the c component of \mathbf{k} , Eqs. (3.5) hold even in the presence of a surface.

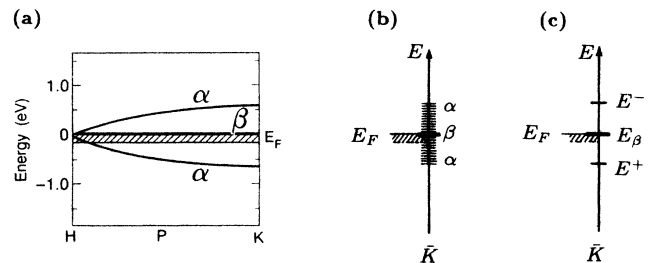


FIG. 8. Schematic band structure along the *P* line in the bulk Brillouin zone (a) and at \bar{K} in the surface BZ of hexagonal graphite (b), and at \bar{K} in the surface BZ of rhombohedral graphite (c). Also shown is a typical energy interval scanned by STM.

The only nonvanishing matrix element is between α sites in adjacent layers,

$$H_{\alpha\alpha'} = (e^{+i\pi\xi} + e^{-i\pi\xi})V_{\alpha\alpha'} = 2V_{\alpha\alpha'}\cos(\pi\xi) = t_\alpha(\xi). \quad (3.5f)$$

Thus the Hamilton matrix reads

$$H(\frac{1}{3}, \frac{1}{3}, \xi) = \begin{matrix} & \alpha & \alpha' & \beta & \beta' \\ \begin{matrix} \alpha \\ \alpha' \\ \beta \\ \beta' \end{matrix} & \begin{bmatrix} E_{p_z} & t_\alpha(\xi) & 0 & 0 \\ t_\alpha(\xi) & E_{p_z} & 0 & 0 \\ 0 & 0 & E_{p_z} & 0 \\ 0 & 0 & 0 & E_{p_z} \end{bmatrix} \end{matrix}. \quad (3.6)$$

Along the P line, this Hamiltonian gives rise to a doubly

degenerate band at $E = E_{p_z}$ near E_F , with wave functions localized on the β sites, and to a dispersive band with wave functions localized on the α sites [Fig. 8(a)].^{23,24} The STM, which scans a narrow energy region near E_F corresponding to \mathbf{k} states near the P line, detects all β states and only a very small fraction of the α states. It is this “density-of-states” effect, rather than a different spatial extension of wave functions on neighboring sites,²⁵ which causes an asymmetry in the STM current between adjacent carbon sites.

The extension of this physical picture from the bulk to the (0001) surface is simple. The P line in the bulk Brillouin zone collapses to the point $\bar{K} = (\frac{1}{3}, \frac{1}{3})$ in the two-dimensional surface BZ [Fig. 8(b)]. The two-dimensional Wigner-Seitz cell has infinitely many atoms, giving rise to a semi-infinite Hamilton matrix. Denoting the sites in the topmost layer by α, β , those in the second layer by α', β' , etc., we find at \bar{K}

$$H(\frac{1}{3}, \frac{1}{3}) = \begin{matrix} & \alpha & \alpha' & \alpha'' & \cdots & \beta & \beta' & \beta'' & \cdots \\ \begin{matrix} \alpha \\ \alpha' \\ \alpha'' \\ \vdots \\ \beta \\ \beta' \\ \beta'' \\ \vdots \end{matrix} & \begin{bmatrix} E_{p_z} & t_\alpha & 0 & \cdots & 0 & 0 & 0 & \cdots \\ t_\alpha^* & E_{p_z} & t_\alpha & \cdots & 0 & 0 & 0 & \cdots \\ 0 & t_\alpha^* & E_{p_z} & \cdots & 0 & 0 & 0 & \cdots \\ \vdots & \vdots & \vdots & \ddots & \vdots & \vdots & \vdots & \ddots \\ 0 & 0 & 0 & \cdots & E_{p_z} & 0 & 0 & \cdots \\ 0 & 0 & 0 & \cdots & 0 & E_{p_z} & 0 & \cdots \\ 0 & 0 & 0 & \cdots & 0 & 0 & E_{p_z} & \cdots \\ \vdots & \vdots & \vdots & \ddots & \vdots & \vdots & \vdots & \ddots \end{bmatrix} \end{matrix}. \quad (3.7)$$

We note that this is a block matrix with a tridiagonal α submatrix and a diagonal β submatrix, describing linear chains of interacting α atoms and isolated β atoms. Electronic states, which formed the α band along the P line in the bulk BZ, now fold to a continuum at \bar{K} , which is spread over approximately 1.2 eV around $E_{p_z} \approx E_F$. The β band folds essentially to a δ function at E_F .²⁴ The physical origin of the asymmetry in the tunneling current between the α and the β sites is unchanged. Since the local density of states on α and β sites is symmetric around E_F , we predict—at least in our simplified model—no dependence of the observed asymmetry on the polarity of the bias voltage.

As the magnitude of the bias voltage is increased, the tunneling process samples states increasingly far from the P line (or \bar{K} point), where α and β states are not completely decoupled. However, because of the large band dispersion near P or \bar{K} , the part of the BZ sampled by the STM is still very small, which causes a decrease, but not a disappearance, of the asymmetry for larger bias voltages V .

This behavior can be quantified by using the definition of the asymmetry A in Eq. (2.5). The tight-binding mod-

el then predicts A to be positive (implying that the STM observes mainly β -type atoms), to decrease with increasing V , and to be independent of the polarity of V . Since the inequivalence of α and β sites with respect to the neighbors in adjacent layers exists both in the bulk and at the surface of hexagonal graphite, the asymmetry should show a similar behavior in these two cases. Thus the tight-binding model explains the asymmetry behavior obtained in the *ab initio* calculation (see Fig. 6) and observed in the experiment.⁵

B. Rhombohedral and other forms of graphite

The tight-binding model can also be used to interpret the STM charge-density asymmetry, which has been calculated on surfaces of rhombohedral graphite (Fig. 7). The Fermi surface is again very close to the \bar{K} point in the surface BZ [Fig. 2(b)]. For $\bar{K} = (\frac{1}{3}, \frac{1}{3})$, all matrix elements of the Hamiltonian can be similarly evaluated as in the section on hexagonal graphite. We find that the only nonvanishing off-diagonal matrix element is between α sites in one layer and β sites in the adjacent layer below.

The corresponding Hamilton matrix reads

$$H\left(\frac{1}{3}, \frac{1}{3}\right) = \begin{matrix} & \alpha & \beta & \alpha' & \beta' & \alpha'' & \beta'' & \cdots \\ \begin{matrix} \alpha \\ \beta \\ \alpha' \\ \beta' \\ \alpha'' \\ \beta'' \\ \vdots \end{matrix} & \begin{bmatrix} E_{p_z} & 0 & 0 & t_\alpha & 0 & 0 & \cdots \\ 0 & E_{E_{p_z}} & 0 & 0 & 0 & 0 & \cdots \\ 0 & 0 & E_{p_z} & 0 & 0 & t_\alpha & \cdots \\ t_\alpha^* & 0 & 0 & E_{p_z} & 0 & 0 & \cdots \\ 0 & 0 & 0 & 0 & E_{p_z} & 0 & \cdots \\ 0 & 0 & t_\alpha^* & 0 & 0 & E_{p_z} & \cdots \\ \vdots & \vdots & \vdots & \vdots & \vdots & \vdots & \vdots \end{bmatrix} \end{matrix} \quad (3.8)$$

The eigenstates of this operator are those of carbon dimers $\alpha\beta'$, $\alpha'\beta''$, etc., which are decoupled from each other and also from the topmost layer β sites. The spectrum, shown in Fig. 8(c), consists of bonding (E^+) and antibonding (E^-) carbon dimer levels, and of a symmetry-induced surface state at E_F , localized on surface β sites. Hence, if the tunneling current should originate from \bar{K} only, the STM should image only the β atoms through this surface state at small bias voltages. At larger bias voltages of the order of several tenths of a volt, the large asymmetry should decrease abruptly to a much smaller value. Also in rhombohedral graphite, we expect no dependence of the asymmetry on the polarity of the bias voltage.

However, unlike in hexagonal graphite, the fundamental gap closes nearly to zero energy away from \bar{K} ,^{15,26} so that the Fermi surface contains also bulk states and a large portion of the tunneling current will come from those bulk states even at low bias voltages. Thus, the suggested abrupt decrease of A , as predicted on the basis of the Hamiltonian in Eq. (3.8), is expected to be washed out. This is indeed the case in the result of our *ab initio* calculation shown in Fig. 7.

In graphite with AA layer stacking, which occurs in stage-1 graphite intercalation compounds in nature, any site asymmetry of the tunneling current, of course, disappears. On graphite surfaces with an arbitrary stacking sequence, the surface density of states and asymmetry between adjacent sites will be essentially determined by the stacking sequence of a few topmost layers. Thus we expect that STM images of any graphite surface should closely resemble one of the graphite structures discussed above.

IV. DISCUSSION AND CONCLUSIONS

The interpretation of the observed tunneling current $j(\mathbf{r})$ in terms of local densities of states, as suggested in Ref. 10 and used in Eq. (2.1), is based on several assumptions, which may be an oversimplification of the real experimental situation. The shape of the tungsten tips currently used in experiment is likely not to be spherical and the relevant electronic states of the tip may not be exclusively s waves with a constant density of states. Furthermore, changes in the tunneling matrix element

occur when the tip-to-surface distance is not constant (such as in the topographic or constant current mode) or if the bias voltage is changed. Since the tunneling matrix element depends so strongly on the experimental conditions (tip shape and distance from the surface, which are unknown), we do not attempt to calculate absolute current densities. In the present work, we rather calculate STM charge densities $\rho_{\text{STM}}(\mathbf{r}, V)$, defined in Eq. (2.2a). For a constant tip-to-surface separation and low bias voltages, the tunneling matrix element, which determines the proportionality constant in Eq. (2.1),¹⁰ is not likely to be very sensitive to the lateral tip position. Then, the STM charge densities $\rho_{\text{STM}}(\mathbf{r}, V)$, calculated in planes parallel to the surface, may be compared to the relative changes in the tunneling current $j(x, y, z = \text{const})$ observed in the current imaging (constant distance) mode.

We find that the observed asymmetry between neighboring carbon sites on hexagonal graphite originates from the special symmetry of the electronic states near the \bar{K} point in the surface Brillouin zone. We do not find surface states to be important for the interpretation of the observed asymmetry on the hexagonal graphite surface. We find that the general trend of decreasing A [Eq. (2.5)] with increasing V holds even for large negative bias voltages, corresponding to tunneling into unoccupied graphite states. For V between -1.3 and -2.5 V, the asymmetry is negligibly small (of the order of 10^{-2}). A previous calculation⁹ obtained an increase of the asymmetry at -1.3 V, which is at variance with our result. Quantitatively correct predictions for such large bias voltages, however, must include consideration of voltage-dependent tunneling matrix elements, and such calculations require the knowledge of the tunneling barrier. Also, new experimental difficulties arise in this voltage range, since the graphite surface tends to disintegrate under the influence of large electric fields.

The physical picture for the asymmetry of rhombohedral graphite is quite different from that for hexagonal graphite. p_z orbits on surface β atoms are decoupled from p_z orbitals of all other atoms in the crystal at \bar{K} and form a surface state there. It is this surface-state band which causes the large asymmetry at low bias voltages, shown in Fig. 7.

As discussed in Ref. 8, the STM images and observed asymmetries can vary considerably for different tips and samples. The experimental data shown in Fig. 6 were obtained for the same tip and sample, at different voltages, and correspond to the largest values observed. Also, the independence of the asymmetry on the bias polarity was observed by switching the polarity in the middle of one scan. It seems plausible that images with lower lateral resolution would be obtained by relatively large, irregular tips. Since a finite lateral resolution also imposes an upper limit on the maximum value of the observable asymmetry, we expect the observed asymmetries to be smaller than the calculated values, which correspond to an infinitely sharp tip. This is consistent with the result of comparing theoretical and experimental data in Fig. 6, especially in the voltage range corresponding to large asymmetries.

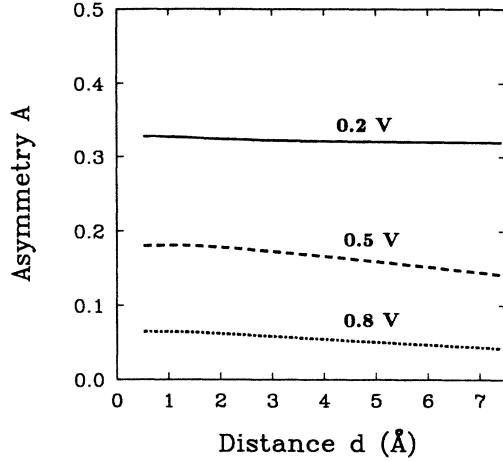


FIG. 9. Results of a tight-binding model calculation for the dependence of the asymmetry $A \equiv [j(\beta) - j(\alpha)] / [j(\beta) + j(\alpha)]$ of the tunneling current j on the tip-to-surface separation d for bias voltages -0.2 V, -0.5 V, and -0.8 V.

Since the tip-to-surface separation in the experiment is not known, we perform our calculation at tip distances of 0.5 and 1 Å and find very small changes in the asymmetry A in this distance range. (A similar result has been found previously in a study of the “giant” corrugations.⁷) At substantially larger distances to the surface (few angstroms), which might correspond to realistic tip-to-surface separations, A is expected to decrease, as discussed in Ref. 10. The extremely low charge-density values in that region are very difficult to obtain accurately in a self-consistent calculation.

To get an estimate of the dependence of A on the tip-to-surface separation d , we performed a tight-binding calculation of $\rho_{\text{STM}}(\mathbf{r}, V)$ for the surface of hexagonal graphite, along the lines of the formalism used in Sec. III. The expansion coefficients $c_{nj}(\mathbf{k})$ ($j = \alpha, \alpha', \beta, \beta'$) for $\psi_{n\mathbf{k}}$ in Eq. (3.1) were obtained by performing a band-structure calculation for a 20-layer slab. At each site, s , p_x , p_y , and p_z orbitals were included. The on-site energies and values for the Slater-Koster²⁷ parameterized hopping integrals were obtained by fitting the band structure of bulk graphite. We used $E_s = -7.3$ eV, $E_p = 0.0$ eV for the on-site energies, $V_{ss\sigma} = -4.30$ eV, $V_{sp\sigma} = 4.98$ eV, $V_{pp\sigma} = 6.38$ eV, and $V_{pp\pi} = -2.66$ eV for the intralayer nearest-neighbor interactions. For the interaction between α sites in adjacent layers, we adjusted the value of $V_{pp\sigma}$ to give the correct splitting at \bar{K} and scaled the other interactions accordingly, which yielded $V_{ss\sigma} = -0.18$ eV, $V_{sp\sigma} = 0.21$ eV, $V_{pp\sigma} = 0.27$ eV, and $V_{pp\pi} = -0.11$ eV. The hopping integrals between α and β atoms in adjacent layers have been obtained from the latter parameters using a $1/r^2$ distance dependence. The radial distance dependence of the s and p orbitals used in the calculations of the charge density from the Bloch functions $\Phi_j(\mathbf{r}, \mathbf{k})$ in Eq. (3.2) was obtained from an atomic calculation. At \bar{K} , the charge density due to pure p_z states has a node on α sites for all values of d . This explains the large value of A

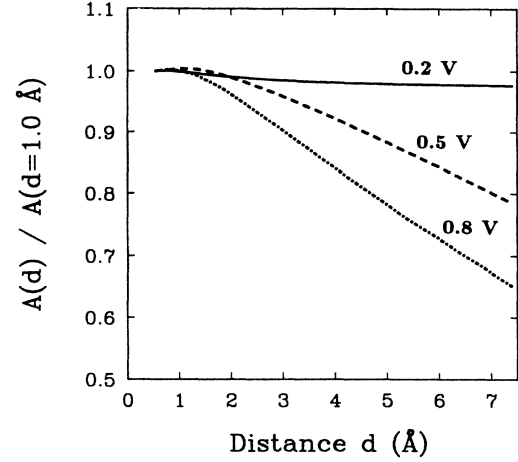


FIG. 10. Relative dependence of the asymmetry $A(d)$, shown in Fig. 9, on the tip-to-surface separation d and bias voltage V .

and its weak distance dependence at low bias voltages. With increasing bias voltage, states from an increasingly large portion of the Brillouin zone contribute to ρ_{STM} , which causes smoothening of the charge density due to those states and, as a consequence, a reduction of the asymmetry as well as a more rapid decrease in A as a function of distance. This is shown in Figs. 9 and 10. Since the values of the asymmetry at large distances are comparable to those at 0.5 Å (see Fig. 10), the results of our *ab initio* calculation are relevant for the interpretation of the experimental data. The present tight-binding model has serious limitations, such as considering only nearest-neighbor interactions or approximating the charge distribution of an embedded carbon atom by that of an isolated atom. In spite of these limitations, the agreement with the *ab initio* and experimental results confirms our main understanding of the system.

In summary, we have investigated the surfaces and the bulk of graphite with different layer stacking sequences using first-principles calculations. We predicted that STM experiments should observe a strong asymmetry in the tunneling current between adjacent carbon sites on surfaces of hexagonal and rhombohedral graphite, while no asymmetry should exist on a model stage-1 (AA stacking) intercalated graphite surface. We find that STM should image preferentially surface atoms with no neighbors in the adjacent layer below. The asymmetries should be largest and polarity independent at small bias voltage, and should decrease with increasing values of the bias voltage. The physical origin of this effect is explained within a simple tight-binding Hamiltonian by the unique symmetry of the states near \bar{K} in the surface Brillouin zone near the Fermi energy. Hence, the asymmetry has an electronic and not a structural origin. Many of these predictions for the case of hexagonal graphite have been verified by observations.

ACKNOWLEDGMENTS

We thank S. Fahy for stimulating discussions and for making his results for graphite available prior to publication. Stimulating comments of J. Tersoff concerning the distance dependence of the asymmetry are also gratefully acknowledged. We thank J. Clarke and co-workers for communicating their experimental results prior to publi-

cation and for valuable discussions. This work was supported by the Director, Office of Energy Research, Office of Basic Sciences, Materials Sciences Division of the U.S. Department of Energy, under Contract No. DE-AC03-76SF00098. Cray computer time at the National Magnetic Fusion Energy Computer Center was provided by the U.S. Office of Energy Research of the Department of Energy. One of us (S.G.L.) wishes to acknowledge the support of the Miller Institute.

*Present address: Department of Physics and Astronomy and Center for Fundamental Materials Research, Michigan State University, East Lansing, MI 48824-1116.

¹G. Binnig, H. Rohrer, Ch. Gerber, and E. Weibel, *Phys. Rev. Lett.* **49**, 57 (1982).

²A. Bryant, D. P. E. Smith, and C. F. Quate, *Appl. Phys. Lett.* **48**, 832 (1986).

³R. V. Coleman, B. Drake, P. K. Hansma, and G. Slough, *Phys. Rev. Lett.* **55**, 394 (1985); Sang-II Park and C. F. Quate, *Appl. Phys. Lett.* **48**, 112 (1986); P. K. Hansma, *Bull. Am. Phys. Soc.* **30**, 251 (1985).

⁴G. Binnig, H. Fuchs, Ch. Gerber, H. Rohrer, E. Stoll, and E. Tosatti, *Europhys. Lett.* **1**, 31 (1986).

⁵H. J. Mamin, E. Ganz, D. W. Abraham, R. E. Thomson, and J. Clarke, *Phys. Rev. B* **34**, 9015 (1986).

⁶J. M. Soler, A. M. Baro, N. Garcia, and H. Rohrer, *Phys. Rev. Lett.* **57**, 444 (1986).

⁷J. Tersoff, *Phys. Rev. Lett.* **57**, 440 (1986).

⁸D. Tománek, S. G. Louie, H. J. Mamin, D. W. Abraham, E. Ganz, R. E. Thomson, and J. Clarke, *Phys. Rev. B* **35**, 7790 (1987).

⁹A. Selloni, P. Carnevali, E. Tosatti, and C. D. Chen, *Phys. Rev. B* **31**, 2602 (1985).

¹⁰J. Tersoff and D. R. Hamann, *Phys. Rev. Lett.* **50**, 1998 (1983); *Phys. Rev. B* **31**, 805 (1985).

¹¹P. Hohenberg and W. Kohn, *Phys. Rev.* **136**, B864 (1964).

¹²W. Kohn and L. J. Sham, *Phys. Rev.* **140**, A1133 (1965).

¹³C. T. Chan, D. Vanderbilt, and S. G. Louie, *Phys. Rev. B* **33**, 2455 (1986); **34**, 8791(E) (1986).

¹⁴N. A. W. Holzwarth, S. G. Louie, and S. Rabii, *Phys. Rev. B* **26**, 5382 (1982), and references therein.

¹⁵S. Fahy, S. G. Louie, and M. L. Cohen, *Phys. Rev. B* **34**, 1191 (1986).

¹⁶S. Fahy (private communication).

¹⁷D. R. Hamann, M. Schlüter, and C. Chiang, *Phys. Rev. Lett.* **43**, 1494 (1979).

¹⁸L. Hedin and B. J. Lundqvist, *J. Phys. C* **4**, 2064 (1971).

¹⁹A. Baratoff (private communication), and unpublished.

²⁰The presence of a position-insensitive offset current could modify the magnitude of the observed asymmetry.

²¹H. Lipson and A. R. Stokes, *Proc. R. Soc. London, Ser. A* **181**, 101 (1942).

²²N. A. W. Holzwarth, S. G. Louie, and S. Rabii, *Phys. Rev. B* **28**, 1013 (1983), and references therein.

²³The degeneracy lifting in the π bands along the P line due to interlayer interactions has been discussed previously, e.g., by J. C. Slonczewski and P. R. Weiss, *Phys. Rev.* **109**, 272 (1958), and by J. P. LaFemina and J. P. Lowe, *Int. J. Quant. Chem.* **30**, 769 (1986).

²⁴The dispersion of the β states due to second-nearest-neighbor plane interactions, which determines the shape of the graphite Fermi surface, is very small, as shown in Ref. 14, and can safely be neglected in the present qualitative discussion of the STM results.

²⁵C. F. Quate, *Phys. Today* **39**(8), 26 (1986).

²⁶R. R. Haering, *Can. J. Phys.* **36**, 352 (1958).

²⁷J. C. Slater and G. F. Koster, *Phys. Rev.* **94**, 1498 (1954).

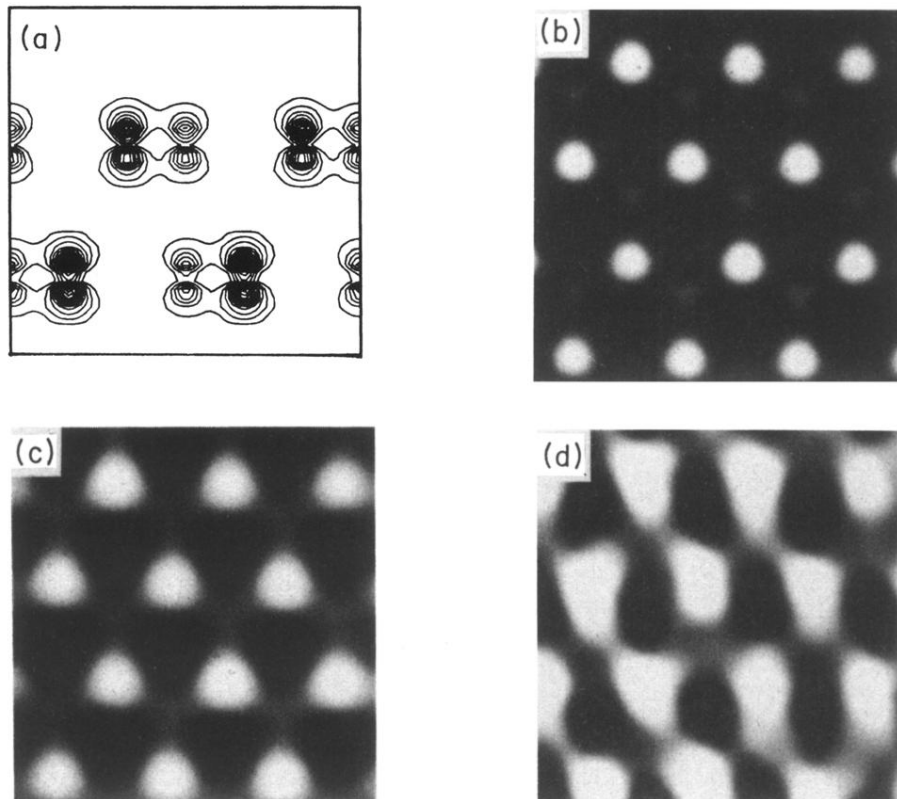


FIG. 4. Comparison of theoretical STM charge density to experimental tunneling current density at hexagonal graphite surfaces for a bias voltage of 0.25 V. Calculated values are shown in a plane perpendicular (a) and parallel (b) to the graphitic layers at a distance 1 Å from the topmost layer. (c) is obtained by filtering high-frequency Fourier components of the charge density of (b) with a Gaussian, can be compared to experimental data from Ref. 8, shown in (d). On the gray scale, white regions correspond to large current densities.